# Integration of Layered Group IV Selenides: From SnSe-$SnSe_{2-x}S_x$ Core-Shell Crystals to Complex (SnSe-$SnSe_{2-x}S_x$)-GeSe van der Waals Heterostructures

Eli Sutter[1,2,*] and Peter Sutter[3]

[1]Department of Mechanical & Materials Engineering, University of Nebraska-Lincoln, Lincoln, Nebraska 68588, United States

[2]Nebraska Center for Materials and Nanoscience, University of Nebraska-Lincoln, Lincoln, NE 68588, United States

[3]Department of Electrical & Computer Engineering, University of Nebraska-Lincoln, Lincoln, Nebraska 68588, United States

## Abstract

The layered semiconductor tin selenide (SnSe) has received extensive interest due to its promising thermoelectric and ferroelectric properties. Integrating SnSe with other layered crystals in heterostructures can enable the modification of charge- and thermal transport, electrical polarization, and other properties such as chemical stability, optoelectronics, and photonics. Here, we demonstrate the vapor transport synthesis of single-crystalline SnSe monochalcogenide flakes that are spontaneously encapsulated in a thin layered $SnSe_{2-x}S_x$ dichalcogenide shell. In a second growth step, such SnSe-$SnSe_{2-x}S_x$ heterostructures are integrated with the monochalcogenide GeSe, which is laterally stitched to the SnSe side facets while preserving the dichalcogenide shell across the basal facets. This architecture is confirmed by optical microscopy, electron microscopy and diffraction, energy dispersive X-ray and Raman spectroscopies, as well as cathodoluminescence spectroscopy. The results extend our capabilities for materials integration by forming complex heterostructures with both vertical van der Waals interfaces and covalent lateral interfaces between layered semiconductors.

*Corresponding author: esutter@unl.edu

**Keywords:** 2D layered crystals, tin selenide, germanium selenide, heterostructures, interfaces, lateral epitaxy

## 1. Introduction

Tin selenide (SnSe), a layered group IV chalcogenide, has received attention due to its promise as an exceptional thermoelectric material with low lattice thermal conductivity between 600 K and 800 K and a large thermoelectric figure of merit *zT*.[1-3] SnSe has also attracted interest as a van der Waals ferroelectric,[4, 5] for applications as an anode material for sodium-ion batteries,[6] and for optoelectronics as a semiconductor with anisotropic orthorhombic structure and ~0.9 eV indirect bandgap,[7] *e.g.*, for self-powered photodetectors.[8] Layered SnSe flakes of different sizes and thicknesses have been prepared on mica and $SiO_2$/Si substrates using a wide range of growth conditions *via* vapor transport using an SnSe precursor. Deposition temperatures ranged between 340°C[9, 10] and 550°C[11], while the SnSe source powder was heated to 500°C[9] to 650°C.[10] Some high-yield synthesis was performed at temperatures as high as 950°C for long periods of time (up to 180 minutes)[12] but the formation of thinner flakes generally requires low temperatures.[4] Occasionally $SnO_2$ and Se were used as precursors, providing control over the selection of selenides with different stoichiometry (either SnSe or $SnSe_2$) depending on the $SnO_2$/Se ratio,[13] but also requiring higher evaporation temperatures (850°C for $SnO_2$).

Monolayer and few-layer heterostructures between SnSe and other 2D materials have been sought after, similar to heterostructures between other 2D crystals that have been studied intensely due to the promise of emergent properties and improvement of device performance.[14] For example, calculations predict that lateral heterostructures between SnSe and SnTe should be promising for photovoltaic applications.[15] So far, vertically stacked SnSe-black phosphorus heterostructures have been realized, showing promise for memristors,[16] while SnSe-$MoSe_2$ heterojunctions may find use as photocatalysts.[17]

Combining SnSe with tin dichalcogenides, such as $SnSe_2$, $SnS_2$, or chalcogen-substituted $SnSe_{2-x}S_x$ alloys, promises the realization of a *pn* heterojunction between naturally *n*-type dichalcogenides and *p*-type SnSe.[18] Coexistence of mono- and dichalcogenides can be achieved by partial thermal[18] or electron beam[19] conversion of $SnSe_2$ to SnSe. Consecutive deposition creates SnSe-$SnSe_2$ junctions in films that have shown promise as photoelectrochemical photodetectors,[20] nanosheet SnSe-$SnSe_2$ long-cyclic anodes for Li-ion batteries,[21] $NO_{2[22]}$ and methanol vapor[23] sensors. Introducing a nanometer scale $SnSe_2$ secondary phase appears to lower the thermal conductivity of SnSe, thus increasing its thermoelectric figure of merit.[24, 25] Ordered heterostructures with well-defined interfaces between SnSe and $SnSe_2$, however, are still lacking.

Another intriguing architecture are lateral heterostructures. Calculations for 2D SnSe-GeSe heterostructures predict type-*II* band alignment and a direct bandgap, with strong optical absorption intensity that can reach the order of $10^5$ $cm^{-1}$, photoelectric conversion efficiency of 21.47%, and a high hole mobility of $6.42 \times 10^4$ $cm^2$ $V^{-1}$ $s^{-1}$ of the heterostructure along the *a*-direction, creating prospects for applications in solar cells[26] and nanomechanics.[27] However, SnSe and GeSe appear difficult to integrate, giving rise to SnSe nanosheet stacks attached to GeSe rather than well-aligned lateral heterostructures.[28]

Here we use vapor transport to grow few-layer to multilayer SnSe flakes. We investigate the structure of the flakes and conclude that they are single crystals that spontaneously encapsulate during growth in a thin ordered $SnSe_2$ shell with traces of S, *i.e.*, form SnSe-$SnSe_{2-x}S_x$ core-shell crystals. These structures not only promise passivation of the SnSe core, but they represent wrap-around SnSe-$SnSe_{2-x}S_x$ heterostructures with diverse interface geometries for optoelectronics and other applications. A second (GeSe) growth step transforms such seed crystals into complex van

der Waals heterostructures in which the (001) basal facets of the SnSe flakes remain terminated by a layered $SnSe_{2-x}S_x$ dichalcogenide while the part of the shell covering the {110} side facets is replaced by crystalline GeSe bands that are laterally stitched to the SnSe flakes. Transmission electron microscopy (TEM), energy dispersive X-ray spectroscopy (EDS), Raman spectroscopy, and cathodoluminescence in scanning TEM (STEM-CL) are used to investigate the structure and morphology of these heterostructures. Our results identify approaches for transforming layered SnSe flakes into complex van der Waals architectures and for modifying their properties by interface formation and integration with other layered semiconductors.

## 2. Results and Discussion

Vapor transport using a SnSe powder precursor yields SnSe flakes on HOPG and Si substrates (for details of the growth process, see the Methods). TEM images of typical SnSe flakes are shown in Figure 1 (a), (a'). The flakes have large lateral sizes that can exceed 20 μm. The overall shape is characterized by an almost square footprint, bounded by long straight {110} side facets and a large (001) top facet (as determined from electron diffraction, Figure 1 (e)), similar to SnS flakes.[29] The flakes also frequently show truncated corners (Figure 1 (a)) due to fast growth along the [100] direction.[30] High-resolution TEM and electron diffraction confirm that the flakes consist of monocrystalline SnSe. TEM images within the (001) facet of the flakes show a stripe moiré pattern (Figure 1 (c)). Figure 1 (d) shows that the stripe pattern is superimposed on the SnSe lattice fringes, characteristic of a moiré pattern of parallel-stacked SnSe and $SnSe_2$ sheets with well-defined relative azimuthal orientation (Figure S2). In addition, imaging near the edges show a layered structure consisting of ~2-4 "standing" layers (Figure S1), in which the van der Waals stacking is perpendicular to the stacking direction in the bulk of the SnSe flake. These

findings suggest the spontaneous formation of a layered core-shell structure in which a single-crystalline SnSe core is surrounded by a thin wrap-around shell of layered $SnSe_2$, similar to the structure of SnS flakes grown with a small excess of sulfur.[29, 31]

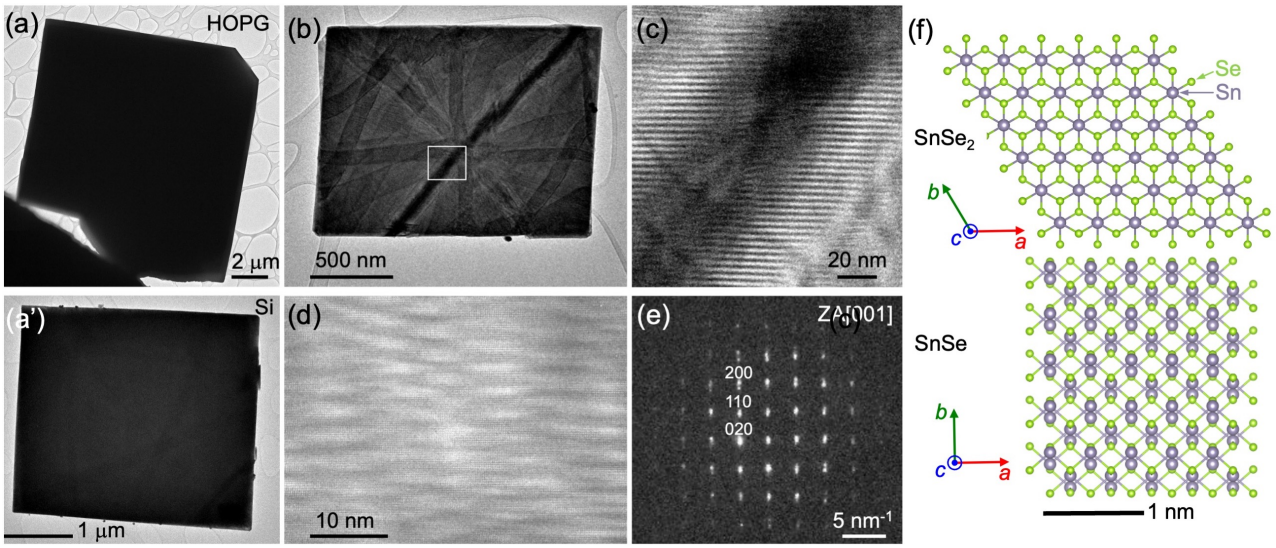


**Figure 1. Growth of SnSe on HOPG and Si substrates. (a), (a'), (b)** TEM images of SnSe flakes grown on HOPG and Si after transfer to lacey carbon grid. **(c)** TEM image showing a stripe moiré pattern across the (001) basal facet of the SnSe flakes (white rectangle in (b)). **(d)** High-resolution TEM of the moiré pattern recorded in the darker area in (c) showing the underlying lattice structure of SnSe. **(e)** Nanobeam electron diffraction pattern from the central area of the SnSe flake (zone axis: [001]). (f) Ball-and-stick models of the crystal structures of $SnSe_2$ (top) and SnSe (bottom).

SnSe seed crystals grown on HOPG, as discussed in the previous section, were converted into multilayer SnSe-GeSe heterostructures by deposition of GeSe in a second growth step (see Methods for details). TEM imaging of SnSe-GeSe heterostructures with different thicknesses shows distinct contrast between the SnSe center and a newly formed peripheral GeSe band (Figure 2). TEM analysis establishes that the width of the GeSe band ranges between 1.5 – 2 μm, independent of the size of the SnSe seed flake (which typically falls between 3.4 – 7 μm). The width of the GeSe band is similar for SnSe flakes with different thicknesses.

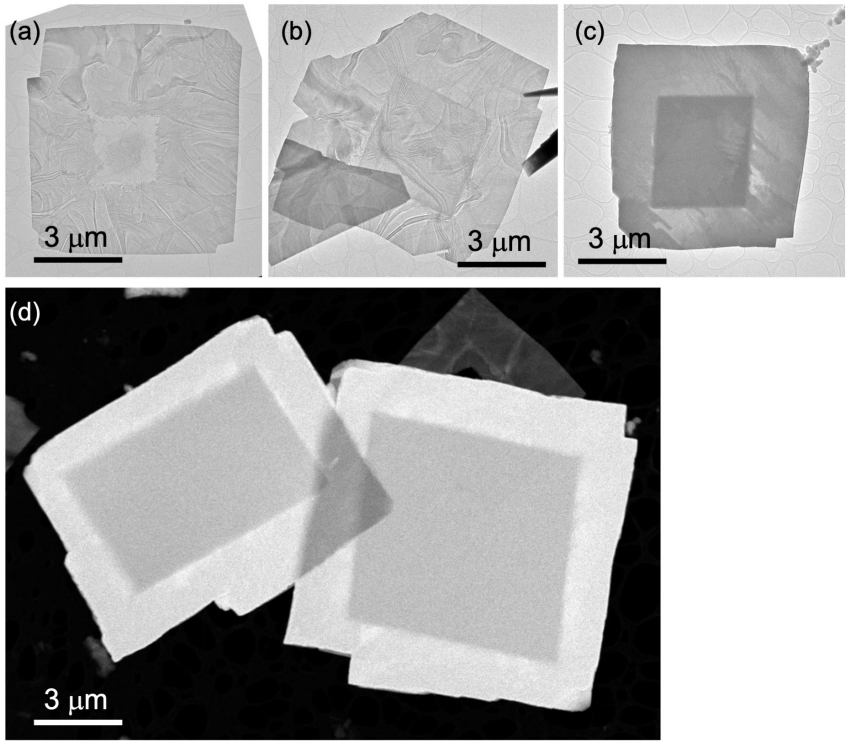


**Figure 2. SnSe-GeSe heterostructures. (a) – (c)** TEM and **(d)** HAADF-STEM images of SnSe-GeSe heterostructures with different thicknesses grown on HOPG substrates.

Micro-Raman spectroscopy was used to further investigate the GeSe-SnSe heterostructures. An optical image of a typical SnSe-GeSe flake is shown in Figure 3 (a). Raman linescans across such flakes detect the vibrational modes of GeSe in the periphery (Figure 3 (b), (d)),[32] while the center shows primarily the vibrational modes of SnSe (Figure 3 (d)).[10, 11, 33, 34] In addition to the SnSe modes, the Raman linescans across the central region show a peak (marked * in the spectrum from the SnSe center, Figure 3 (c)) that does not originate from SnSe. This extra peak is close to the frequency to both the $A_g$ peak of GeSe and to the $A_{1g}$ mode of $SnSe_2$. GeSe can be ruled out as the source of this peak; if it were caused by the presence of GeSe across the top of the SnSe flake, then all three GeSe modes – or at least the substantially stronger $B_{3g}$ mode – should be present. Comparison of parts of the linescan across the GeSe and SnSe regions, however, indicates that the three GeSe modes are not detected in the center, suggesting a different origin for this peak.

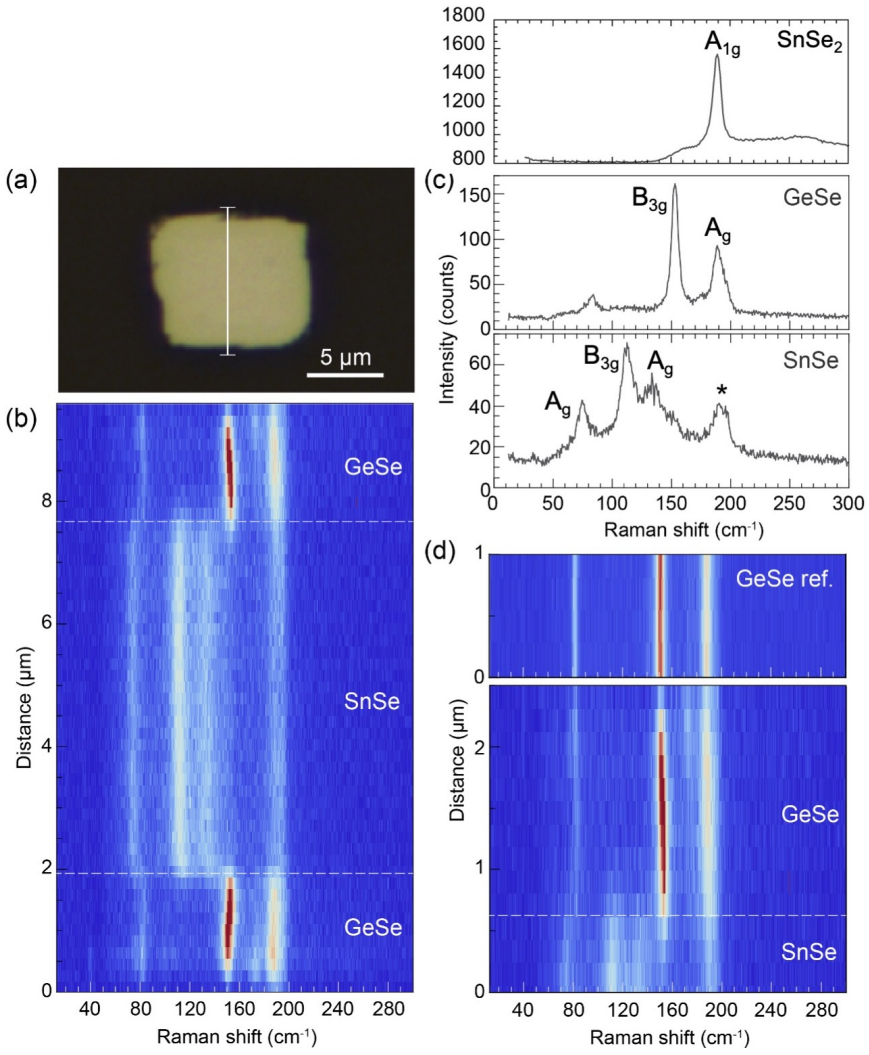


**Figure 3. Raman analysis of characteristic SnSe-GeSe heterostructures. (a)** Optical microscopy of a SnSe-GeSe heterostructure. **(b)** Raman linescan across the heterostructure, as shown in (a). **(c)** Raman spectra from the SnSe center of the heterostructure, from the GeSe edge band and from an $SnSe_2$ crystal reference. **(d)** Raman linescan from the GeSe edge band and the vicinity to the SnSe interface compared to reference linescan on a pure GeSe ribbon.

Taking into account the observation of a moiré pattern in the SnSe flakes and of a wrap-around shell prior to the GeSe growth step, we assign this peak to the most intense ($A_{1g}$) mode of $SnSe_2$. The presence of this Raman peak therefore confirms that the $SnSe_2$ shell across the top of the SnSe flake remains also after GeSe growth.[35, 36] Note, however, that the $A_{1g}$ mode is slightly blue-shifted (by 2-3 $cm^{-1}$) from its frequency in bulk $SnSe_2$ (Figure 3 (c)), similar to Raman shifts observed in $SnSe_xS_{2-x}$ alloys with low sulfur content,[37] indicating that it might contain

some sulfur. Additional chemical analysis, discussed below, provides further evidence for alloying with S from traces of residual sulfur present in the growth reactor.

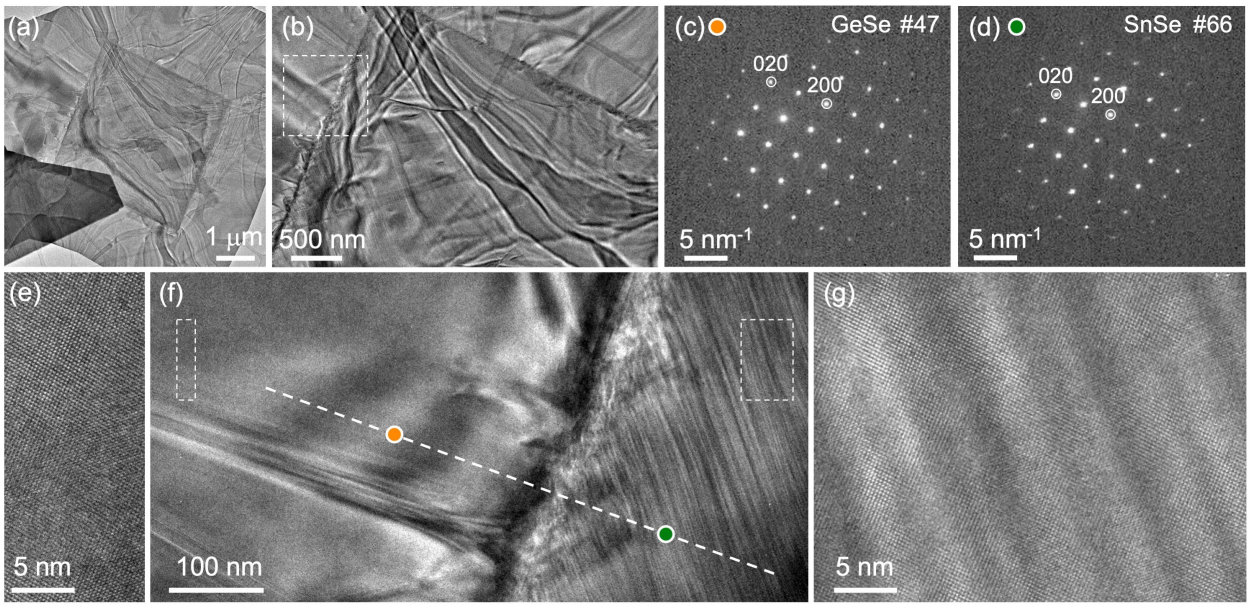


**Figure 4. High-resolution TEM and nanobeam electron diffraction of SnSe-GeSe lateral heterostructures. (a)** TEM image of a SnSe-GeSe heterostructure. **(b)** Higher magnification TEM from an area close to the SnSe-GeSe interface. **(c), (d)** Selected nanobeam electron diffraction patterns (DPs) from a series of 100 DPs obtained across the SnSe-GeSe interface (along the dashed line in (f), with a step of 10 nm). **(e)** High-resolution TEM images of the GeSe peripheral band (rectangle in (f), left side). **(f)** Detail view of the SnSe-GeSe interface (area marked in (b)). **(g)** High-resolution TEM image of the SnSe seed flake showing a stripe-moiré pattern (rectangle in (f), right side).

Structure and morphology of the heterostructures were investigated by TEM and electron diffraction (Figure 4, Figure S3). Figure 4 (a) shows a heterostructure consisting of a thin, nearly square SnSe flake with 3.6 µm × 3.6 µm lateral dimensions and a peripheral band of 1.4 – 1.7 µm width with different contrast, consistent with GeSe attached to the edges of the SnSe seed flake. The lateral SnSe-GeSe heterostructure preserves and extends the faceted shape of the initial SnSe seed. Nanobeam electron diffraction linescans across the lateral interface (Figure 4 (c), (d)) confirm the center as single-crystalline SnSe (diffraction pattern (DP) #66) while the peripheral band consists of single-crystalline GeSe (DP #47). Electron diffraction patterns of the GeSe component (Fig. 4 (c), #47) identify the sharp corners to be along the ⟨100⟩ directions

while the facets of the truncated corners align along the ⟨010⟩ directions, similar to the shapes observed for homogeneous GeSe flakes. In Figure 4 and Figure S3, both the SnSe and GeSe components of the heterostructure are imaged along the [001] zone axis and DPs show their lattices aligned, similar to SnS-GeS[38, 39] and SnS-GeSe heterostructures.[40] High-resolution TEM confirms the high crystal quality of both the SnSe seed and the peripheral GeSe band (Figure 4 (e), (g)). The TEM images show that the peripheral GeSe band is uniform and single phase, while the center shows a stripe moiré pattern similar to the original SnSe seed flakes (Figure 1) with wrap-around Sn-dichalcogenide shells. In the DPs from the SnSe core (Fig. 4 (d)) there are noticeable additional diffraction spots, likely due to the thin $SnSe_2$ (or $SnSe_{2-x}S_x$, see below) covering the surface. Figure S3, however, shows a more complicated stripe moiré pattern and a number of diffraction spots in addition to those stemming from the main material. In the immediate vicinity of the GeSe interface there is a darker moiré band with triple diffraction spots, which then transitions into the homogeneous stripe moiré pattern that corresponds to the SnSe-$SnSe_{2-x}S_x$ vertical stack. The darker band results from some vertical overgrowth of GeSe from the lateral interface across parts of the SnSe-$SnSe_{2-x}S_x$ stack, as identified by the EDS line scan in Figure S4 (f).[38] Whereas in GeSe-SnS heterostructures GeSe attaches exclusively at the SnS edge (resulting in pure edge growth without creating a capping layer as found for SnS-GeS heterostructures),[38, 39] it appears that for SnSe flakes the GeSe peripheral growth extends locally over the SnSe core in the vicinity of the SnSe-GeSe interface. The extent of overgrowth is not identical in all investigated heterostructures, but it varies from very narrow (below 20 nm, Figure 4 (a)) to wider (up to ~800 nm (Figure 2 (a)) in different heterostructures.

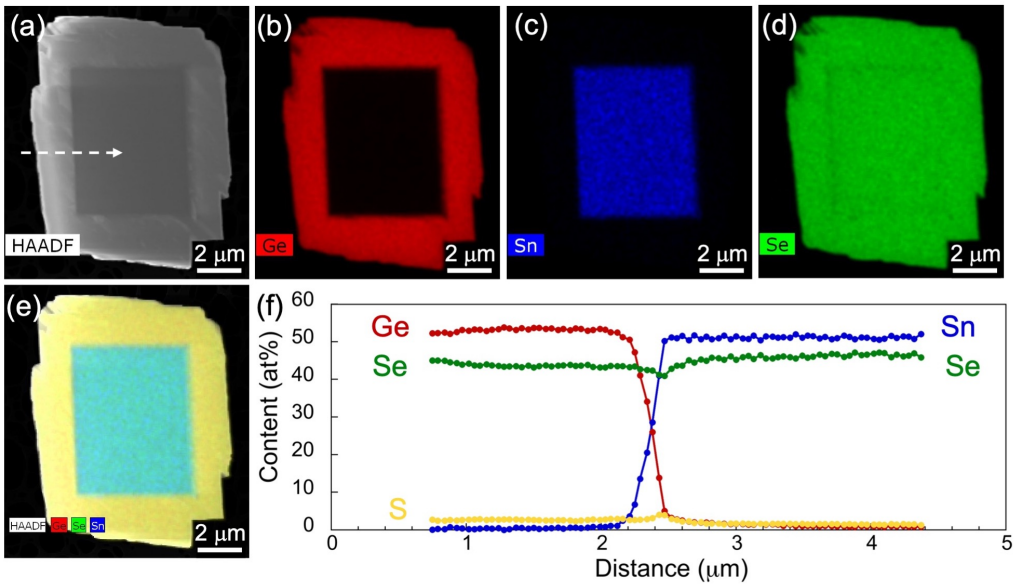


**Figure 5. Elemental maps obtained by energy dispersive X-ray spectroscopy (EDS) in STEM. (a)** HAADF-STEM image of a characteristic SnSe-GeSe lateral heterostructure. **(b) – (d)** Elemental maps showing the distribution of Ge (b), Sn (c), and Se (d) in the heterostructure. **(e)** Compound map showing all major elements of the heterostructure. **(f)** EDS linescan across the lateral interface between SnSe and GeSe (arrow in (a)).

STEM-EDS maps, spectra, and linescans were used to analyze the composition in the core and the peripheral band, as well as across the lateral interface. Figure 5 (a) – (e) shows EDS maps of the elemental distribution in a typical heterostructure. Maps and linescans show that the core consists of Sn and Se. In the peripheral band, Ge and Se are detected as the major constituents (Figure 5 (b), (d)) while Sn is below the detection limit (Figure 5 (f)). Additionally, sulfur is detected throughout the entire heterostructure. The GeSe portion of the heterostructure contains ~2.7 at.% S. The SnSe seed at the center of the heterostructure contains ~1.5 at.% S. At the interface, there is a peak in the S content (~3 at.%), likely due to sulfur enrichment during the thermal decomposition of the mixed dichalcogenide shell across the side facets prior to GeSe growth. This explanation is consistent with prior results, which showed a substantially lower onset temperature for Se loss from $SnSe_2$ than for S loss from $SnS_2$.[41] The reduction of the dichalcogenide shell across the side facets is a prerequisite for high-quality lateral epitaxy of GeSe on the SnSe seeds with the observed lattice alignment. The interfacial S-enrichment also

moderates the difference in lattice parameters between the SnSe and GeSe parts of the heterostructures. In heterostructures with larger extent of GeSe overgrowth over the SnSe-$SnSe_{2-x}S_x$ seed, EDS allows the detection of the locally vertically stacked GeSe in the vicinity of the heterointerface (Figure S4). The linescan across the interface in this particular heterostructure demonstrates a higher Ge content near the lateral SnSe-GeSe interface that extends ~400 nm over the SnSe seed, beyond which the Ge content decreases to below the detection limit.

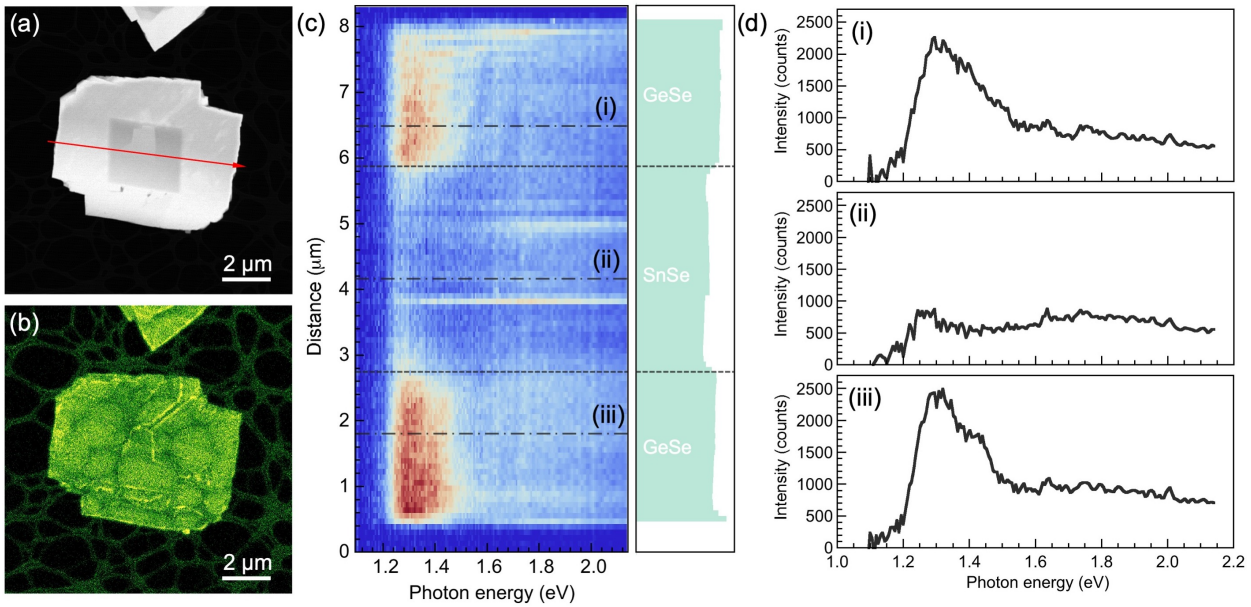


**Figure 6. STEM cathodoluminescence of SnSe-GeSe lateral heterostructures. (a)** STEM image of a SnSe-GeSe lateral heterostructure. **(b)** Panchromatic STEM-CL image of the heterostructure in (a). **(c)** Hyperspectral CL linescan across the heterostructure (red arrow in (a)). The plot on the right shows the STEM intensity along the scan line. **(d)** Local CL spectra showing the predominant peaks in the GeSe side band of the heterostructure at the positions marked by the dashed lines (i) and (iii) and in the SnSe center (dashed line (ii)). Note the absence of light emission from SnSe due to limitations of the measurement to the visible/near-infrared part of the spectrum, precluding detection of the band-edge emission at 0.94 eV (see Figure S5).

The optoelectronic properties of the SnSe-GeSe heterostructures were investigated using cathodoluminescence spectroscopy in scanning transmission electron microscopy (STEM-CL), measured on individual flakes. The panchromatic STEM-CL map of a heterostructure (Figure 6) shows relatively uniform light emission. Hyperspectral linescans across the heterostructure were used to analyze the spectral distribution of the luminescence. In the peripheral GeSe band we

find a wide emission peak characteristic of the band-edge luminescence of GeSe, which consists of two distinct peaks corresponding to the fundamental indirect bandgap along the Γ-Y direction (1.27 eV, GeSe) and a slightly larger direct bandgap at the Γ-point.[40] Measurements at low temperatures (104 K) give rise to narrower emission peaks (Figure S5), from which the bandgap was determined to be 1.32 eV. This value is ~30 meV higher than the bandgap of pure GeSe at 104 K (1.29 eV).[32] We ascribe this increase in the bandgap to the S-incorporation in the GeSe portion of our heterostructures (see Figure 5). We recently established that for the GeSe-GeS system, the bandgap changes nearly linearly between the gaps of the end compounds GeSe (1.27 eV) and GeS (1.58 eV). Thus, incorporation of 2.7 at% S should result in an increase of the band gap by ~10 meV.[42] In the central part of the flake, no luminescence peaks are observed. Since in our STEM-CL system, the detectable photon energy range is limited to ~1.2 – 3.5 eV, this indicates that any emission from SnSe is limited to the band-edge luminescence at photon energy below the detectable range, without any radiative transitions at higher energy. Indeed, UV-Vis-NIR absorption measurements, performed in diffuse scattering geometry on dense arrays of SnSe on the original Si growth substrates, determine the optical bandgap as ~0.94 eV (Fig. S6), consistent with values reported in the literature for bulk crystals[43] and flakes.[12]

## 3. Conclusion

In summary, we used vapor transport synthesis and characterization by electron microscopy and Raman spectroscopy to demonstrate the formation of single-crystalline SnSe monochalcogenide flakes that are spontaneously encapsulated in a thin layered $SnSe_{2-x}S_x$ dichalcogenide shell (with trace S content below ~3 at.%) during growth from a SnSe powder precursor. The spontaneous encapsulation of crystalline SnSe flakes in a thin $SnSe_{2-x}S_x$ shell is of interest in the context of thermoelectrics since prior work showed that decoration with $SnSe_2$ can significantly increase the carrier concentration and decrease the thermal conductivity of SnSe.[24,

25] Furthermore, the self-encapsulation of SnSe may carry other benefits such as preventing surface oxidation, which is found to have a detrimental effect on the thermoelectric properties of the material.[44, 45] In fact underperformance of polycrystalline SnSe appears to be largely due to oxidation, and oxide reduction allows recovering the ZT of single crystals in polycrystalline samples.

We also demonstrate lateral stitching of the monochalcogenides SnSe and GeSe (comprising the few-layers to multilayer thickness range) in heterostructures, using a two-step growth process involving SnSe seed flake growth followed by lateral epitaxy of GeSe. Analysis by optical and electron microscopy and diffraction, EDS and Raman spectroscopy confirms the formation of a lateral SnSe-GeSe heterostructure. The SnSe-$SnSe_{2-x}S_x$ wrap-around morphology of the original flakes is preserved during the GeSe deposition step, albeit only across the basal (001) facets. The tight integration of SnSe and GeSe along the lateral interface and the high crystal quality of GeSe with lattice aligned to the SnSe seed suggests that the $SnSe_{2-x}S_x$ shell covering the side facets of the SnSe seed flake was reduced and eliminated during the initial GeSe growth. The final heterostructures show a predominant lateral integration of crystalline GeSe and SnSe, with vertical GeSe overgrowth limited to the immediate vicinity of the lateral interface. Cathodoluminescence shows band-edge emission consistent with high-quality GeSe within the peripheral band while no detectable emission above ~1.2 eV photon energy is observed across SnSe, consistent with an optical gap of ~0.94 eV. We conclude that our two-step growth process produces complex heterostructure architectures, in which the (001) facets of monocrystalline SnSe seed flakes are terminated by a thin $SnSe_{2-x}S_x$ shell, while wide single crystalline bands consisting of layered GeSe are covalently bonded to the {110} side facets. Such heterostructures carry promise for modifying the electronic structure, charge and thermal transport in SnSe, and

they add to the capabilities for materials integration by forming vertical van der Waals interfaces as well as sharp covalent lateral interfaces between layered semiconductors.

## 4. Experimental Methods

*Growth step I – Encapsulated SnSe seed flakes on graphite and Si substrates.* Large multilayer SnSe seed crystals were synthesized in a pumped quartz tube reactor with two independently controlled temperature zones. SnSe source powder (99.999%, ALB Materials) was placed in a quartz boat in the center of the evaporation zone and heated to 550-600°C. A freshly cleaved graphite substrate (MTI Crystal) was placed in the second temperature zone and heated to a growth temperature of 460°C. During growth, a carrier gas (Ar, 99.9999%, Matheson) was maintained at a flow of 60 standard cubic centimeters per minute (sccm) and a pressure of 20 mTorr. Growth was typically performed for 30 minutes, after which the reactor was cooled naturally to room temperature.

*Growth step II – Formation of GeSe-SnSe heterostructures.* GeSe was deposited on the SnSe seeds *via* vapor transport from a pure GeSe precursor (99.99%, ALB Materials) in a reactor with two independently controlled temperature zones. The evaporation zone containing a quartz boat with GeSe powder (~25 mg) was heated to a temperature of 400-420°C, while the zone containing the SnSe seeds on graphite was heated to 320°C. During growth, an Ar (99.9999%, Matheson) carrier gas was maintained at a flow of 60 sccm and a pressure of 20 mTorr. GeSe growth was typically performed for 15 minutes, after which the reactor was cooled naturally to room temperature. Occasionally the growth time was extended to obtain wider GeSe rims (see for example Figure 7).

*Optical microscopy, Raman spectroscopy, and spectrophotometry.* Optical microscopy and micro-Raman spectroscopy/mapping were performed in air in an optical/Raman microscope

(Horiba Xplora Plus). Raman spectroscopy was performed with a 100× objective at 532 nm excitation wavelength and 16.8 μW laser power. Raman spectra and linescans were measured using a 300 μm pinhole at ~0.5 μm spatial resolution. The optical absorption of as-grown SnSe flake ensembles on Si substrate was measured in a diffuse reflectance geometry using a Perkin-Elmer Lambda-750 spectrophotometer equipped with 100 mm InGaAs integrating sphere.

*Electron microscopy, nanobeam diffraction, cathodoluminescence spectroscopy, energy dispersive X-ray spectroscopy, and TEM sample preparation.* Structure and morphology of the heterostructures were investigated by (scanning) transmission electron microscopy ((S)TEM) and nanobeam electron diffraction in an FEI Talos F200X field emission microscope. STEM-cathodoluminescence (STEM-CL) was performed using a Gatan Vulcan CL holder at 200 keV electron energy and an incident beam current of ~400 pA. Panchromatic CL maps (512 × 512 pixels, 1.28 ms per pixel) were acquired by scanning the exciting electron beam and recording the emitted light intensity over a broad wavelength range (400-1000 nm). Hyperspectral linescans were acquired by displacing the electron beam in equal steps across individual heterostructures and acquiring full CL spectra (integration time: 10 s per spectrum) at each beam position. Energy-dispersive X-ray spectroscopy (EDS) was carried out in an FEI Tecnai Osiris microscope at 200 keV. For plan-view (S)TEM, SnSe-GeSe heterostructures were transferred from graphite or Si substrates to TEM grids using stabilization by spin-coated (3000 rpm, 60 s) poly(methyl methacrylate) (PMMA) films, baked at 70°C for 5 minutes, followed by release of the heterostructure/PMMA sandwich by de-ionized water penetration.[46] After pickup by a TEM grid the PMMA film was dissolved by immersion in acetone, leaving GeSe-SnSe heterostructures on the grid.

**Supporting Information:** Electron microscopy of SnSe flakes; light absorption in SnSe, TEM, electron diffraction, and EDS spectroscopy of SnSe-GeSe heterostructures.

**Acknowledgements.** This work was supported by the U.S. Department of Energy, Office of Science, Office of Basic Energy Sciences under Grant DE-SC0023437. EDS measurements were performed in the Nebraska Nanoscale Facility: National Nanotechnology Coordinated Infrastructure and the Nebraska Center for Materials and Nanoscience, which are supported by the National Science Foundation under Award ECCS: 2025298, and the Nebraska Research Initiative.

**Conflict of Interest.** The authors declare no competing interests.

**Data Availability Statement.** The data that support the findings of this study are available from the corresponding author upon reasonable request.

## References


[1] L.-D. Zhao, S.-H. Lo, Y. Zhang, H. Sun, G. Tan, C. Uher, C. Wolverton, V.P. Dravid, M.G. Kanatzidis, Ultralow thermal conductivity and high thermoelectric figure of merit in SnSe crystals, Nature, 508 (2014) 373-377.

[2] L.-D. Zhao, C. Chang, G. Tan, M.G. Kanatzidis, SnSe: a remarkable new thermoelectric material, Energy Environ Sci, 9 (2016) 3044-3060.

[3] C. Chang, G. Tan, J. He, M.G. Kanatzidis, L.-D. Zhao, The Thermoelectric Properties of SnSe Continue to Surprise: Extraordinary Electron and Phonon Transport, Chem Mater, 30 (2018) 7355-7367.

[4] M.-H. Chiu, X. Ji, T. Zhang, N. Mao, Y. Luo, C. Shi, X. Zheng, H. Liu, Y. Han, W.L. Wilson, Z. Luo, V. Tung, J. Kong, Growth of Large-Sized 2D Ultrathin SnSe Crystals with In-Plane Ferroelectricity, Adv Electron Mater, 9 (2023) 2201031.

[5] Y. Luo, N. Mao, D. Ding, M.-H. Chiu, X. Ji, K. Watanabe, T. Taniguchi, V. Tung, H. Park, P. Kim, J. Kong, W.L. Wilson, Electrically switchable anisotropic polariton propagation in a ferroelectric van der Waals semiconductor, Nat Nanotechnol, 18 (2023) 350-356.

[6] X. Ren, J. Wang, D. Zhu, Q. Li, W. Tian, L. Wang, J. Zhang, L. Miao, P.K. Chu, K. Huo, Sn-C bonding riveted SnSe nanoplates vertically grown on nitrogen-doped carbon nanobelts for high-performance sodium-ion battery anodes, Nano Energy, 54 (2018) 322-330.

[7] M. Parenteau, C. Carlone, Influence of temperature and pressure on the electronic transitions in SnS and SnSe semiconductors, Phys Rev B, 41 (1990) 5227-5234.

[8] B. Ouyang, C. Chang, L.-D. Zhao, Z.L. Wang, Y. Yang, Thermo-photoelectric coupled effect induced electricity in N-type SnSe:Br single crystals for enhanced self-powered photodetectors, Nano Energy, 66 (2019) 104111.

[9] S. Zhao, H. Wang, Y. Zhou, L. Liao, Y. Jiang, X. Yang, G. Chen, M. Lin, Y. Wang, H. Peng, Z. Liu, Controlled synthesis of single-crystal SnSe nanoplates, Nano Res, 8 (2015) 288-295.

[10] X. Xu, Q. Song, H. Wang, P. Li, K. Zhang, Y. Wang, K. Yuan, Z. Yang, Y. Ye, L. Dai, In-Plane Anisotropies of Polarized Raman Response and Electrical Conductivity in Layered Tin Selenide, ACS Appl Mater Interf, 9 (2017) 12601-12607.

[11] S. Luo, X. Qi, H. Yao, X. Ren, Q. Chen, J. Zhong, Temperature-Dependent Raman Responses of the Vapor-Deposited Tin Selenide Ultrathin Flakes, J Phys Chem C, 121 (2017) 4674-4679.

[12] L. Qiu, X. Lai, J. Jian, Substrate-independent growth and characterization of single-crystalline SnSe nanoplates, Mater Charact, 172 (2021) 110864.

[13] Z. Wang, F. Pang, A facile way to control phase of tin selenide flakes by chemical vapor deposition, Chem Phys Lett, 702 (2018) 90-95.

[14] A. Castellanos-Gomez, X. Duan, Z. Fei, H.R. Gutierrez, Y. Huang, X. Huang, J. Quereda, Q. Qian, E. Sutter, P. Sutter, Van der Waals heterostructures, Nat Rev Methods Primers, 2 (2022) 58.

[15] Q. Zhuang, J. Li, C. He, T. Ouyang, C. Zhang, C. Tang, J. Zhong, Type-II lateral SnSe/GeTe heterostructures for solar photovoltaic applications with high efficiency, Nanoscale Adv, 3 (2021) 3643-3649.

[16] H. Tian, X. Cao, Y. Xie, X. Yan, A. Kostelec, D. DiMarzio, C. Chang, L.-D. Zhao, W. Wu, J. Tice, J.J. Cha, J. Guo, H. Wang, Emulating Bilingual Synaptic Response Using a Junction-Based Artificial Synaptic Device, ACS Nano, 11 (2017) 7156-7163.

[17] Y. Cheng, J. Zhang, C. Chen, X. Xiong, J. Zeng, J. Xi, Y.-J. Yuan, Z. Ji, A novel 2D/2D $MoSe_2$/SnSe heterojunction photocatalyst with large carrier transmission channel shows excellent photoelectrochemical performance, Appl Surf Sci, 563 (2021) 150311.
[18] Z. Tian, M. Zhao, X. Xue, W. Xia, C. Guo, Y. Guo, Y. Feng, J. Xue, Lateral Heterostructures Formed by Thermally Converting n-Type $SnSe_2$ to p-Type SnSe, ACS Appl Mater Interf, 10 (2018) 12831-12838.
[19] E. Sutter, Y. Huang, H.P. Komsa, M. Ghorbani-Asl, A.V. Krasheninnikov, P. Sutter, Electron-Beam Induced Transformations of Layered Tin Dichalcogenides, Nano Lett, 16 (2016) 4410-4416.
[20] C. Lu, W. Dong, Y. Zou, Z. Wang, J. Tan, X. Bai, N. Ma, Y. Ge, Q. Zhao, X. Xu, Direct Z-Scheme $SnSe_2$/SnSe Heterostructure Passivated by $Al_2O_3$ for Highly Stable and Sensitive Photoelectrochemical Photodetectors, ACS Appl Mater Interf, 15 (2023) 6156-6168.
[21] W. Feng, X. Wen, Y. Wang, L. Song, X. Li, R. Du, J. Yang, H. Li, J. He, J. Shi, Interfacial Coupling $SnSe_2$/SnSe Heterostructures as Long Cyclic Anodes of Lithium-Ion Battery, Adv Sci, 10 (2023) 2204671.
[22] X. Wang, Y. Liu, J. Dai, Q. Chen, X. Huang, W. Huang, Solution-Processed p-SnSe/n-$SnSe_2$ Hetero-Structure Layers for Ultrasensitive $NO_2$ Detection, Chem Eur J, 26 (2020) 3870-3876.
[23] Y. Qin, S. Chen, Y. Bai, Adsorption and Sensing Performance toward Methanol Vapor on SnS/$SnS_2$ In-Plane Heterostructures, ACS Appl Electron Mater, 4 (2022) 158-167.
[24] L. Cao, J. Pan, H. Zhang, Y. Zhang, Y. Wu, Y.-Y. Lv, X.-j. Yan, J. Zhou, Y.B. Chen, S.-h. Yao, Y. Pei, M.-h. Lu, Y.-f. Chen, One-Order Decreased Lattice Thermal Conductivity of SnSe Crystals by the Introduction of Nanometer $SnSe_2$ Secondary Phase, J Phys Chem C, 123 (2019) 27666-27671.
[25] B. Qin, Y. Zhang, D. Wang, Q. Zhao, B. Gu, H. Wu, H. Zhang, B. Ye, S.J. Pennycook, L.-D. Zhao, Ultrahigh Average ZT Realized in p-Type SnSe Crystalline Thermoelectrics through Producing Extrinsic Vacancies, J Amer Chem Soc, 142 (2020) 5901-5909.
[26] Y. Mao, C. Xu, J. Yuan, H. Zhao, A two-dimensional GeSe/SnSe heterostructure for high performance thin-film solar cells, J Mater Chem A, 7 (2019) 11265-11271.
[27] H. Ni, M. Li, Y. Hu, C. Mao, L. Xue, H. Zeng, Z. Yan, Y. Wu, C. Zheng, Two-dimensional SnSe/GeSe van der Waals heterostructure with strain-tunable electronic and optical properties, J Phys Chem Solids, 131 (2019) 223-229.
[28] D. Sun, R.E. Schaak, Solution-Mediated Growth of Two-Dimensional SnSe@GeSe Nanosheet Heterostructures, Chem Mater, 29 (2017) 817-822.
[29] P. Sutter, J. Wang, E. Sutter, Wrap-Around Core–Shell Heterostructures of Layered Crystals, Adv Mater, 31 (2019) 1902166.
[30] E. Sutter, J. Wang, P. Sutter, Nanoparticle-Templated Thickness Controlled Growth, Thermal Stability, and Decomposition of Ultrathin Tin Sulfide Plates, Chem Mater, 31 (2019) 2563-2570.
[31] E. Sutter, J. Wang, P. Sutter, Surface Passivation by Excess Sulfur for Controlled Synthesis of Large, Thin SnS Flakes, Chem Mater, 32 (2020) 8034-8042.
[32] E. Sutter, J.S. French, P. Sutter, Free-standing large, ultrathin germanium selenide van der Waals ribbons by combined vapor–liquid–solid growth and edge attachment, Nanoscale, 14 (2022) 6195-6201.

[33] X. Gong, H. Wu, D. Yang, B. Zhang, K. Peng, H. Zou, L. Guo, X. Lu, Y. Chai, G. Wang, X. Zhou, Temperature dependence of Raman scattering in single crystal SnSe, Vib Spectrosc, 107 (2020) 103034.
[34] H.R. Chandrasekhar, R.G. Humphreys, U. Zwick, M. Cardona, Infrared and Raman spectra of the IV-VI compounds SnS and SnSe, Phys Rev B, 15 (1977) 2177-2183.
[35] A.J. Smith, P.E. Meek, W.Y. Liang, Raman scattering studies of $SnS_2$ and $SnSe_2$, J Phys C: Solid State Phys, 10 (1977) 1321.
[36] D.G. Mead, J.C. Irwin, Raman spectra of $SnS_2$ and $SnSe_2$, Solid State Commun, 20 (1976) 885-887.
[37] J. Yu, C.-Y. Xu, Y. Li, F. Zhou, X.-S. Chen, P.-A. Hu, L. Zhen, Ternary $SnS_{2-x}Se_x$ Alloys Nanosheets and Nanosheet Assemblies with Tunable Chemical Compositions and Band Gaps for Photodetector Applications, Sci Rep, 5 (2015) 17109.
[38] E. Sutter, J. Wang, P. Sutter, Lateral Heterostructures of Multilayer GeS and SnS van der Waals Crystals, ACS Nano, 14 (2020) 12248-12255.
[39] E. Sutter, R.R. Unocic, J.-C. Idrobo, P. Sutter, Multilayer Lateral Heterostructures of Van Der Waals Crystals with Sharp, Carrier–Transparent Interfaces, Adv Sci, 9 (2022) 2103830.
[40] P. Sutter, H.-P. Komsa, K. Kisslinger, E. Sutter, Lateral Integration of SnS and GeSe van der Waals Semiconductors: Interface Formation, Electronic Structure, and Nanoscale Optoelectronics, ACS Nano, 17 (2023) 9552-9564.
[41] T. Shimada, F.S. Ohuchi, B.A. Parkinson, Thermal decomposition of $SnS_2$ and $SnSe_2$: Novel molecular-beam epitaxy sources for sulfur and selenium, J Vac Sci Technol A, 10 (1992) 539-542.
[42] E. Sutter, H.-P. Komsa, J.S. French, P. Sutter, Composition Dependence of the Band Gaps of Semiconducting $GeS_xSe_{1-x}$ van der Waals Alloys, Chem Mater, 35 (2023) 6374-6381.
[43] Y. Kim, I.-H. Choi, Optical and electrical properties of GeSe and SnSe single crystals, J Korean Phys Soc, 72 (2018) 238-242.
[44] B. Zhang, A. Li, G. Han, Z. Zhang, K. Peng, X. Gong, X. Zhou, X. Han, Dynamic Epitaxial Crystallization of $SnSe_2$ on the Oxidized SnSe Surface and Its Atomistic Mechanisms, ACS Appl Mater Interf, 12 (2020).
[45] Y.K. Lee, Z. Luo, S.P. Cho, M.G. Kanatzidis, I. Chung, Surface Oxide Removal for Polycrystalline SnSe Reveals Near-Single-Crystal Thermoelectric Performance, Joule, 3 (2019) 719-731.
[46] R. Frisenda, E. Navarro-Moratalla, P. Gant, D. Pérez De Lara, P. Jarillo-Herrero, R.V. Gorbachev, A. Castellanos-Gomez, Recent progress in the assembly of nanodevices and van der Waals heterostructures by deterministic placement of 2D materials, Chem Soc Rev, 47 (2018) 53-68.